

Rotational modulation and long-term evolution of the small-scale magnetic fields of M dwarfs observed with SPIRou

P. I. Cristofari^{1,2,3,*,}, J.-F. Donati³, S. Bellotti^{1,3}, É. Artigau⁴, A. Carmona⁵, C. Moutou³, X. Delfosse⁵, P. Petit³, B. Finocietti^{3,6}, and J. Dias do Nascimento^{2,7}

¹ Leiden Observatory, Leiden University, PO Box 9513, 2300 RA Leiden, The Netherlands

² Center for Astrophysics | Harvard & Smithsonian, 60 Garden Street, Cambridge, MA 02138, United States

³ Univ. de Toulouse, CNRS, IRAP, 14 avenue Belin, 31400 Toulouse, France

⁴ Institut Trottier de recherche sur les exoplanètes, Département de Physique, Université de Montréal, Montréal, Québec, Canada

⁵ Univ. Grenoble Alpes, CNRS, IPAG, 38000 Grenoble, France

⁶ ACRI-ST, 260 route du Pin Montard, BP 234, 06904 Sophia-Antipolis (France)

⁷ Departamento de Física, UFRN, CP 1641, 59072-970, Natal, RN, Brazil

Received Month DD, YYYY; accepted Month DD, YYYY

ABSTRACT

Context. M dwarfs are known to host magnetic fields, impacting exoplanet studies and playing a key role in stellar and planetary formation and evolution. Observational constraints are essential to guide theories of dynamo processes believed to be at the origin of those fields, in particular for fully-convective stars whose internal structure differs from those of partially-convective stars. Observations revealed long-term evolution of the large-scale magnetic field reconstructed with Zeeman-Doppler imaging, and a diversity of their topologies. These large-scale magnetic fields, however, only account for a small amount of the unsigned magnetic flux at the stellar surface that can be probed by directly modeling the Zeeman broadening of spectral lines in unpolarized spectra.

Aims. We aim at investigating the long-term behavior of the average small-scale magnetic field of fully-convective and partially convective M dwarfs with time, and assess our ability to detect rotational modulation and retrieve rotation periods from time series of field measurements derived from unpolarized spectra.

Methods. We perform fits of synthetic spectra computed with ZeeTurbo to near-infrared high-resolution spectra recorded with SPIRou between 2019 and 2024 in the context of the SLS and SPICE large programs. The analysis is performed on the spectra of 2 partially convective (AD Leo, DS Leo) and 3 fully convective (PM J18482+0741, CN Leo, Barnard star) M dwarfs, along with EV Lac whose mass is close to the fully-convective limit. Our analysis provides measurements of the average small-scale magnetic field, which are compared to longitudinal magnetic field and temperature variation measurements (*dTemp*) obtained from the same data.

Results. We were able to detect the rotation period in the small-scale magnetic field series for 4 of the 6 stars in our sample. We find that the average magnetic field can vary by up to 0.3 kG throughout the year (e.g., CN Leo), or of up to 1 kG across rotation phases (e.g., EV Lac). The rotation periods retrieved from longitudinal and small-scale magnetic fields are found in agreement within error bars. *dTemp* measurements are found to anti-correlate with small-scale magnetic field measurements for three stars (EV Lac, DS Leo and Barnard's star).

Conclusions. The results demonstrate our ability to measure rotation periods from high-resolution data from small-scale magnetic field measurements, provided that the inclination of the observed targets is sufficiently large. We observe long-term fluctuations of the average magnetic field that could indicate magnetic cycles in the parent dynamo processes. These long-term variations appear mainly uncorrelated with large-scale magnetic field variations probed through the longitudinal field measurements. Large variations in amplitude of the rotationally modulated signals, in particular, hint towards a change in the distribution of the surface inhomogeneities accessible to Zeeman broadening measurements.

Key words. Techniques: spectroscopic – Stars: low-mass – Stars: magnetic field

1. Introduction

M dwarfs have attracted increasing attention in the past years for their properties as planet hosts. The characterization of M dwarfs is, in particular, essential to establish reliable constraints on the detected planets (Bonfils et al. 2013; Dressing & Charbonneau 2015; Gaidos et al. 2016). M dwarfs are known to host magnetic fields (e.g., Saar & Linsky 1985; Johns-Krull & Valenti 1996; Shulyak et al. 2014; Kochukhov 2021; Reiners et al. 2022), routinely impairing exoplanet characterization, and at the origin of activity phenomena leading to spurious signals in radial velocity

curves (e.g., Dumusque et al. 2021; Bellotti et al. 2022). These fields play a crucial role in stellar formation and evolution (Donati & Landstreet 2009), and are responsible for a number of observable phenomena, such as momentum loss over the stellar life (e.g., Skumanich 1972; Vidotto et al. 2014) that led to the development of gyrochronology (Barnes 2003), or surface inhomogeneities (spots, plages, faculae).

M dwarfs are the most numerous stars in the solar vicinity (Reylé et al. 2021), with masses ranging from 0.08 to 0.57 M_{\odot} (Pecaut & Mamajek 2013). Stars with masses $< 0.35 M_{\odot}$ are predicted to be fully convective. In partially convective stars, with $M > 0.35 M_{\odot}$, the tachocline (region

* cristofari@strw.leidenuniv.nl

at the interface between the inner radiative core and outer convective envelope, Chabrier & Baraffe 1997) has been proposed as a key ingredient in dynamo processes at the origin of magnetic fields. In fully convective stars, dynamo theories can no longer rely on the tachocline, and an alternative α^2 -dynamo mechanism is proposed to generate strong magnetic fields without the need of the tachocline (Chabrier & Küker 2006; Yadav et al. 2015).

In the last decade, the advent of new high-resolution near-infrared instruments, including spectrometers such as CARMENES (Quirrenbach et al. 2014) and spectropolarimeters such as CRIRES+ (Dorn et al. 2023) or SPIRou (Donati et al. 2020), along with the development of new spectral modeling codes, have provided new constraints on the atmospheric properties of a large number of M dwarfs (e.g., Rajpurohit et al. 2018; Passegger et al. 2019; Marfil et al. 2021; Sarmento et al. 2021; Cristofari et al. 2022b,a). The polarized data recorded with such instruments led to numerous studies focused on the large-scale magnetic field of such stars (e.g. Finocietti et al. 2023; Donati et al. 2023a; Bellotti et al. 2024), while several other works relied on unpolarized spectra to estimate the average surface magnetic field of low-mass and Sun-like stars by modeling the Zeeman broadening and intensification of well-selected spectral lines (Shulyak et al. 2017; Reiners et al. 2022; Cristofari et al. 2023a,b; Kochukhov et al. 2024). Those measurements open the door to complementary studies aiming at drawing a complete picture of the magnetic fields in M dwarfs from large-scale and small-scale field measurements (e.g. Kochukhov & Lavail 2017; Donati et al. 2023a). Large surveys of magnetic M dwarfs have produced timeseries of spectra for hundred of stars, providing the data necessary to investigate the link between rotation and magnetic fields. Magnetic activity is known to scale with Rossby number, defined as the ratio between rotation period and convective turnover time, and recent works found that magnetic fields follow a similar trend for fully and partially convective stars (e.g. Reiners et al. 2022; Cristofari et al. 2023b).

In this paper, we present for the first time a systematic investigation of the evolution of the average magnetic field and longitudinal field on periods of months or years for several magnetic M dwarfs observed with SPIRou. We rely on the long-term monitoring of 6 fully-convective and partially-convective targets (EV Lac, DS Leo, CN Leo, PM J18482+0741, AD Leo and Barnard star) with SPIRou. We introduce the observations in Sec. 2 and the tools used for the analysis in Sec 3. In Sec. 4 we present our results, before discussing them in Sec. 6.

2. Observations and reduction

The analysis presented in this paper relies of observations recorded with SPIRou, the spectropolarimètre infrarouge installed at the Canada-France-Hawaii Telescope, in the context of the SPIRou legacy Survey (SLS), a three year program that was allocated 310 nights between 2019 and 2022, of the SPIRou Legacy Survey - Consolidation and enhancement (SPICE) large program, and of observations obtained in the context of PI programs (Run ID 24AC25, 23AD98, 22BF10, 24AF17, 24BF13, and 23BF08). We focus on a sample of 5 strongly magnetic M dwarfs (EV Lac, AD Leo, DS Leo, CN Leo, PM J18482+0741, see Table 1), to which we add one quiet star (Barnard's star). Spectra were reduced with APERO version 0.7.291 (Cook et al. 2022). Wavelength calibration, blaze estimation from flat-field exposures and telluric correction were performed by APERO.

The unpolarized spectral orders were normalized using a low-degree polynomial, corrected for the barycentric Earth radial velocity (BERV), and re-binned on a common wavelength

grid using a cubic interpolation. In addition to the spectra recorded each night, we compute a median spectrum, referred to as ‘template’ in the rest of the paper, by taking the median of each pixel in the barycentric reference frame. For those templates, the signal-to-noise ratio (SNR) per 2 km s^{-1} pixel can reach up to 2000 in the H band.

The polarimetric data were also reduced with the LIBRE-ESPRIT package adapted to SPIRou data (Donati et al. 2020). The polarimetric products were used to compute mean Stokes I and V profiles with least squares deconvolution (LSD, Donati et al. 1997). The longitudinal field estimates (B_ℓ) obtained with these tools were compared to those obtained from the polarimetric products of APERO and the publicly available code LSDpy¹. The two datasets provide similar results, and we therefore rely on the extensively tested LIBRE-ESPRIT implementation which leads to slightly smaller error bars.

3. Data analysis

3.1. Stellar spectra modeling

Our analysis follows the process presented in Cristofari et al. (2023a), that we briefly describe in this section.

We rely on a grid of synthetic spectra computed with ZeeTurbo (Cristofari et al. 2023a) from MARCS model atmospheres (Gustafsson et al. 2008). Our grid spans temperatures ranging from 2700 to 4000 K, $\log g$ from 3.5 to 5.5 and [M/H] from -0.75 to 0.75 dex. For each set of atmospheric parameters, spectra were computed for surface magnetic fields ranging from 0 to 10 kG in steps of 2 kG, assuming that the magnetic field is radial in all points of the photosphere. Every spectrum in the grid was computed assuming local-thermodynamic equilibrium (LTE). We rely on the results of Wende et al. (2009, see Fig. 10 therein) to determine a microturbulent velocity– T_{eff} relation, yielding $v_{\text{mic}} = a T_{\text{eff}}^2 + b T_{\text{eff}} + c$, with $a = 4.4 \times 10^{-7} \text{ km s}^{-1}\text{K}^{-1}$, $b = -2.4020 \times 10^{-3} \text{ km s}^{-1}\text{K}^{-1}$ and $c = 3.5191 \text{ km s}^{-1}\text{K}^{-1}$. The v_{mic} considered in our grid then range from ~ 0.25 to 0.98 km s^{-1} . We note that previous tests showed that imposing $v_{\text{mic}} = 1 \text{ km s}^{-1}$ for all spectra within the grid has a very small impact on the results of our current analysis.

We adopt the same convention as in Cristofari et al. (2023a,b) and model the stellar spectra with a linear combination of the synthetic spectra computed for various magnetic field strengths so that $S = \sum f_i S_i$, with S_i the spectrum for magnetic field i kG and f_i the filling factor associated to that component. Our fitting procedure ensures that $\sum f_i = 1$. To obtain the best fit to the data, we rely on Markov Chain Monte Carlo (MCMC) with the log-likelihood explicited in Cristofari et al. (2023b), and derive the parameters from the posterior distributions.

3.2. Atmospheric characterization

In a first step, we derive the atmospheric parameters and average magnetic fields obtained for each star by applying our process to the templates (see Table 2). This analysis was performed with the same assumptions on $v \sin i$ than Cristofari et al. (2023a), except for Barnard's star, whose $v \sin i$ is set to 0 km s^{-1} (Cristofari et al. 2023b). The retrieved atmospheric properties are in excellent agreement with those derived in our previous study (Cristofari et al. 2023a) performed on earlier version of the templates. Note that we obtain $\log g \approx 5.0$ dex for PM J18482+0741 and CN Leo, larger than in Cristofari et al. (2023a), and closer to the

¹ <https://github.com/folsomcp/LSDpy>

Table 1. Parameters retrieved in the literature for the stars in our sample.

Star	Gliese ID	Spectral type	P_{rot} (d)	$M (M_{\odot})$	$R (R_{\odot})$	τ (d)	R_O
DS Leo	Gl 410	M1.0V	14.0 ± 0.1^1	0.57 ± 0.02	0.53 ± 0.02	38 ± 23	0.37 ± 0.23
AD Leo	Gl 388	M3V	2.2399 ± 0.0006^2	0.42 ± 0.02	0.39 ± 0.02	57 ± 33	0.04 ± 0.02
EV Lac	Gl 873	M4.0V	4.3715 ± 0.0006^2	0.32 ± 0.02	0.31 ± 0.02	76 ± 42	0.06 ± 0.03
Barnard's star	Gl 699	M4V	136 ± 13^3	0.16 ± 0.02	0.185 ± 0.004	125 ± 67	1.09 ± 0.59
PM J18482+0741	...	M5.0V	2.76 ± 0.01^4	0.14 ± 0.02	0.17 ± 0.02	134 ± 71	0.02 ± 0.01
CN Leo	Gl 406	M6V	2.704 ± 0.003^4	0.11 ± 0.02	0.13 ± 0.02	147 ± 79	0.02 ± 0.01

Notes. Masses and radii were taken from Cristofari et al. (2023a,b). Convective turnover times (τ) were computed from the mass with the relation introduced in Wright et al. (2018). The Rossby number is defined as $R_O = P_{\text{rot}}/\tau$.

Ref. – (1) Donati et al. (2008), (2) Morin et al. (2008), (3): Donati et al. (2023b), (4): Díez Alonso et al. (2019),

values expected from radius and mass estimates (5.12 ± 0.13 dex and 5.25 ± 0.17 dex, respectively, see Table 1). Those improvements can be attributed to our refined line list selection, and improvements to the normalization functions. Surface gravity is known to be difficult to constrain for M dwarfs, and line selection has a significant impact on the results. The error bars on reported atmospheric parameters were inflated to account for some of the systematics following Cristofari et al. (2022b).

In a second step, we fix the atmospheric parameters to those derived from the template, and estimate $\langle B \rangle$ from the spectra recorded each night, obtaining a time series of magnetic field measurements for each star. For all stars but Barnard's star, we model the spectra with a combination of magnetic models ranging from 0 to 10 kG in steps of 2 kG. For Barnard's star, only the 0 and 2 kG components were considered.

4. Temporal modulation of the small-scale and large-scale magnetic fields

4.1. Quasi-periodic Gaussian Process fit to the data

Quasi-periodic Gaussian Processes (GP) have become popular to study the evolution of activity of stars and extract rotation periods (see, e.g., Fouqué et al. 2023; Donati et al. 2023a,b).

We investigate the temporal modulation of our data by using a GP regression with a kernel used in previous studies (Angus et al. 2018; Fouqué et al. 2023):

$$\kappa(t_i, t_j) = \alpha^2 \exp \left[-\frac{(t_i - t_j)^2}{2l^2} - \frac{1}{2\beta^2} \sin^2 \left(\frac{\pi(t_i - t_j)^2}{P_{\text{rot}}} \right) \right] + \sigma^2 \delta_{ij} \quad (1)$$

With α the amplitude of the GP, β a smoothing factor, l the decay time, σ the standard deviation of an added uncorrelated white noise and P_{rot} the recurrence period, here assimilated to the rotation period of the star. This flexible model allows one to model complex structures, but can be degenerate, resulting in over-fitting (Angus et al. 2018). For each star, we therefore obtain a fit with wide priors (assuming little knowledge of the GP hyper-parameters).

Our implementation² relies the George (Ambikasaran et al. 2015) Python package and a workflow loosely based on that of Martioli et al. (2022). Our tools explore the parameter space with a Markov Chain Monte Carlo (MCMC), relying on the emcee package (Mackey et al. 2008) to estimate the set of hyper-parameters (see equation 1) and mean value (μ) that lead to the highest likelihood described in Rasmussen & Williams (2006); Foreman-Mackey et al. (2017) and implemented in George.

² <https://github.com/pchristof/star-activity-tools>

For most targets, the minimum reduced χ^2 (χ_r^2) of the GP fit is much lower than one. These likely reflect that the error bars computed for on $\langle B \rangle$ attempt to account for some of the systematics associated with the measurements, and do not reflect relative precision. Given that we are investigating relative variation of the measurements, we re-scale the error bars using the dispersion of the residuals in order to ensure that the minimum reduced χ_r^2 is closer to 1. In the rest of the papers, the errors listed for $\langle B \rangle$ correspond to these re-scaled error bars.

To estimate the parameters leading to the best fit to the data, we search for the combination of hyper-parameters maximizing the likelihood. In order to avoid bias by a single walker's position, we consider the top 1% walkers with highest likelihood, and take the median of these walkers parameters. Our process was applied to $\langle B \rangle$ and B_ℓ measurements. We additionally performed simultaneous GP fits on the series of $\langle B \rangle$ and B_ℓ measurements, with the same rotation period for both GPs. Last but not least, we applied our process to dTemp measurements obtained following Artigau et al. (2024), attempting to capture temperature variations at the stellar surface by relying on changes in stellar line profiles throughout the observation campaign. For each star, we collected the dTemp measurements obtained with a reference temperature closest to those listed in Table 2 (i.e. 4000 K for DS Leo, 3500 K for AD Leo, EV Lac, and Barnard's star, and 3000 K for PM J18482+0741 and CN Leo). The minimum reduced χ_r^2 of the best GP fit to the series dTemp measurements range from 2 to 94, with particularly large values for CN Leo and PM J18482+0741 ($\chi_r^2 = 57$ and $\chi_r^2 = 94$, respectively), likely indicating that the error bars are under-estimated. For dTemp, we therefore re-scaled error bars to ensure that the minimum reduced χ^2 is closer to 1 for the best fits. The results of the GP fits are presented in Tables A.1, A.2, A.3, A.4, A.5 and A.6.

4.2. DS Leo (Gl 410)

DS Leo is one of the most massive and least magnetic star in our sample, with an average field of 0.79 ± 0.02 kG, and around which a possible planetary system was recently detected with these SPIRou data (Carmona et al. 2025). We detect a clear modulation of the magnetic field strength, with a detectable signal at 13.953 ± 0.088 d, consistent with previously reported rotation estimates (Donati et al. 2008). This period is also in very good agreement with that obtained by applying our process on B_ℓ measurements (14.001 ± 0.077 d).

We observe a variation in the amplitude of $\langle B \rangle$, with a minimum reached between July 2021 and early-2022 (see Fig. C.1, available on Zenodo). The amplitude of the signal varies by more than 0.3 kG, going from ~ 0.9 kG in March 2021 to ~ 0.3 kG in July 2021. The amplitude in B_ℓ measurements is also observed

Table 2. Atmospheric parameters and small-scale magnetic field.

Target	T_{eff} (K)	$\log g$ (dex)	[M/H] (dex)	$v \sin i$ (km s $^{-1}$)	i ($^{\circ}$) ^a	ζ_{RT} (km s $^{-1}$) ^b	$\langle B \rangle$ (kG)
DS Leo	3797 ± 30	4.67 ± 0.05	-0.02 ± 0.10	1.5	51 ± 48	3.01 ± 0.07	0.79 ± 0.02
AD Leo	3475 ± 30	4.81 ± 0.05	0.23 ± 0.10	3.0	20 ± 11	2.19 ± 0.15	3.13 ± 0.05
EV Lac	3342 ± 30	4.75 ± 0.05	0.02 ± 0.10	3.0	57 ± 57	4.22 ± 0.14	4.54 ± 0.09
Barnard's star	3300 ± 31	4.71 ± 0.06	-0.54 ± 0.10^c	$< 0.1^d$...	3.79 ± 0.17	0.51 ± 0.08
PM J18482+0741	3102 ± 32	4.97 ± 0.06	0.01 ± 0.10	2.4	40 ± 27	5.51 ± 0.18	1.27 ± 0.14
CN Leo	2912 ± 31	5.00 ± 0.07	0.22 ± 0.11	2.0	55 ± 45	4.94 ± 0.29	3.08 ± 0.26

Notes. Projected rotational velocities ($v \sin i$) for our analyses were taken from Morin et al. (2008) for AD Leo and Reiners et al. (2018) for PM J18482+0741. For CN Leo, EV Lac and DS Leo, $v \sin i$ estimates were taken from Cristofari et al. (2023a), who revised some values based on rotation periods and radii. Inclinations were derived from $v \sin i$, P_{rot} and radii.

a: Inclinations computed assuming a 1.0 km s $^{-1}$ uncertainty on $v \sin i$.

b: In the present analysis, we fixed $v \sin i$ and fit ζ_{RT} . Consequently, broadening that would arise from non-physical or unidentified sources may lead to larger ζ_{RT} estimates.

c: For Barnard's star, we additionally fit for the [α /Fe] parameter (see Cristofari et al. 2022a), yielding: [α /Fe] = 0.09 ± 0.10 dex.

d: Maximum $v \sin i$ assuming an inclination of 90°.

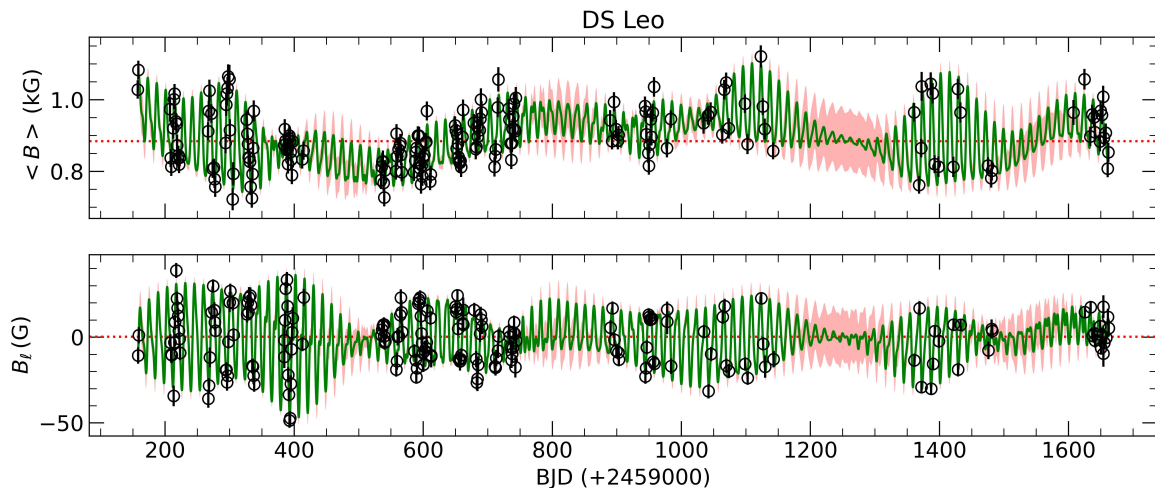


Fig. 1. Simultaneous fit of two GPs on our small-scale and large-scale magnetic fields measurements. The rotational velocity P_{rot} is the same for the two GPs. The pink shaded area shows the uncertainty on the GP fit.

to decrease and then increase, although the minimum is reached in early-2022, and a maximum is reached around July 2021 (see Fig. D.1, available on Zenodo). The series of $\langle B \rangle$ and $|B_\ell|$ appear uncorrelated, yielding a Pearson coefficient of 0.14. GP fits obtained on the time series of filling factors show a clear rotational modulation of the 2 kG component as well as for the non-magnetic component. No clear modulation can be found for the other filling factors whose values are close to 0.

DS Leo was reported to display differential rotation (Hébrard et al. 2016) with rotation periods at the equator and the pole of 13.37 ± 0.86 d and 14.96 ± 1.25 d, respectively. Our period derived from small-scale magnetic field measurements falls between these values.

We carried out a simultaneous fit of two GPs on the series of $\langle B \rangle$ and B_ℓ measurements (see Fig. 1), yielding a rotation period of 13.980 ± 0.059 d, consistent with those derived above. The results of the GP fits are presented in Table A.1.

We applied our process to the $dTemp$ measurements obtained for Gl 410 (see Fig. E.1, available on Zenodo). Our best GP fit to the data yields a well constrained recurrence period $P_{\text{rot}} = 14.214 \pm 0.106$ d (see Table A.1), slightly larger than that estimated from $\langle B \rangle$ and B_ℓ .

4.3. AD Leo

Applying our process to our $\langle B \rangle$ measurements for AD Leo does not provide clear constraints on the rotation period (see Fig. C.2, available on Zenodo). This result can be attributed to the star's low inclination ($i = 19.9 \pm 1.3$ °, see Table 2): throughout the rotation phase, our processes averages out the signal coming from the pole, with very little modulation in the recorded spectra. Our $\langle B \rangle$ measurements remain relatively stable throughout the months and years and little variation in amplitude or mean is observed. Only the first few and last two data points of our series could hint towards a long term decrease of $\langle B \rangle$. The longitudinal field of AD Leo has been shown to vary (Lavail et al. 2018; Bellotti et al. 2023), with a significant increase of the rotationally modulated signal amplitude from mid-2019 to early-2020, and an increase of its mean from early-2020 to mid-2020 (see Fig. D.2, available on Zenodo).

Here again, we perform a simultaneous fit of two GPs to our $\langle B \rangle$ and B_ℓ data. This process yields a rotation period of 2.230 ± 0.001 d, in perfect agreement with that retrieved from B_ℓ (2.230 ± 0.001 d), suggesting that the constraint on P_{rot} primarily arises from B_ℓ . The results of the GP fits are presented in Table A.2.

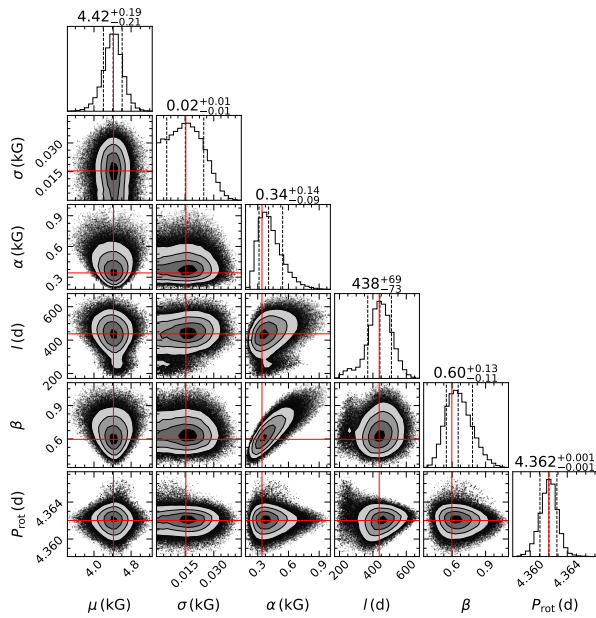


Fig. 2. Posterior distribution of the hyper-parameters obtained for EV Lac. Red lines mark the median of the 1% of walkers which have the highest likelihood.

We perform a fit of a GP on the $dTemp$ measurements. Relying on wide uniform priors yields $P_{\text{rot}} = 1.81 \pm 0.10$ d. We note that two peaks are visible in the posterior distribution with a secondary peak around the expected rotation period. To help convergence, we repeated our process fixing the smoothing parameter to 1.5, and setting a Gaussian prior centered on 2.3 with a 0.3 standard deviation on P_{rot} (see Table A.2). With these additional constraints, we retrieve $P_{\text{rot}} = 2.227 \pm 0.018$ d (see Fig. E.2 and G.14, available on Zenodo). We note that a ~ 1.7 d period is also favored for our GP fit to $\langle B \rangle$ when relying on wide uniform priors, or when setting the decay time to $\beta = 0.4$.

4.4. EV Lac (Gl 873)

We carried out our analysis on data recorded for EV Lac, whose mass places it very close to the generally adopted fully convective boundary (at about $0.35 M_\odot$). Recent investigations have reported the presence of two spots at the stellar surface leading to spurious signals in radial velocity measurements (Larue et al. in prep), and a full stokes spectropolarimetric investigation was recently carried out from the SPIRou data secured in September/October 2023 (Donati et al. 2025). For this star, the atmospheric characterization yields atmospheric parameters in excellent agreement with Cristofari et al. (2023a). Our process provides well constrained GP hyper-parameters (see Fig. 2), and a rotation period of 4.362 ± 0.001 d, very close to that reported by Morin et al. (2008, 4.3715 ± 0.0006 d) and Bellotti et al. (2024, 4.36 ± 0.01 d). This value is also in good agreement with the period retrieved by fitting the GP model to the longitudinal magnetic field measurements (B_ℓ) obtained from polarimetric data, which yields a rotation period of 4.371 ± 0.003 d.

The observations for EV Lac spans ~ 3 years, and a clear fluctuation of GP amplitude is observed, with a minimum in 2019, and a maximum in 2021 (see Fig. 3). The amplitude of the GP decreases again in 2022, while the observations secured in September/October 2023 yield lower mean small-scale field (~ 4.1 kG against ~ 4.5 kG). The amplitude of B_ℓ and $\langle B \rangle$ fol-

low similar trends, with an increase in amplitude of the B_ℓ for the second and fourth seasons, that appear to decrease again in 2022. Comparing the series of $\langle B \rangle$ and $|B_\ell|$, we compute a Pearson correlation coefficient of -0.41 .

The daily sampling of the measurements allows us to observe significant variations in the distribution of the filling factors at different rotation phases (see Fig. 4). These distributions show a clear increase in the 8 kG component in June 22 and June 26/27 2021 corresponding to days where the magnetic field is close to the average value obtained from the template, while the 10 kG component increases on June 23, 24 or 28 when $\langle B \rangle$ is larger than the value estimated from the template. To assess this behavior, we fit a GP on individual filling factors rather than $\langle B \rangle$, restricting the priors around the expected rotation period. For EV Lac, a clear rotation period at 4.361 ± 0.001 d and 4.364 ± 0.003 d is detected for the 2 and 10 kG components, respectively. For the other components, convergence of the GP is more challenging and multiple maxima appear in the rotation period histogram.

We repeat the analysis, simultaneously fitting two GPs to the $\langle B \rangle$ and B_ℓ measurements, with a common rotation period (see Table A.3). The resulting rotation period (4.363 ± 0.001 d) remains closer to that estimated from $\langle B \rangle$ alone than that obtained from B_ℓ . We note that our process applied to $\langle B \rangle$ and B_ℓ converges to significantly different decay times (421 ± 80 d and 125 ± 16 d, respectively).

We additionally fit a GP to the $dTemp$ measurements for EV Lac. Our best fit yields $P_{\text{rot}} = 4.361 \pm 0.001$ d, in excellent agreement with that derived from $\langle B \rangle$. We find that the $dTemp$ obtained from the observations secured in September/October 2023 are on average larger than the measurements obtained on the rest of the data (~ 4 K against -1 K, see Fig. E.3, available on Zenodo), where the small-scale magnetic field becomes weaker. We note the strong anti-correlation between $\langle B \rangle$ and $dTemp$ measurements (see Sec. 5).

4.5. Barnard's star (Gl 699)

To our sample of active M dwarfs, we add Barnard star, a well-known quiet bright M dwarf, with an average magnetic field was estimated to 0.51 ± 0.08 kG (see Table 2). Barnard's star has been extensively studied and is relatively bright, leading to high-quality spectra throughout the monitoring campaign. This star therefore represents an ideal test case to assess the performance of our method on a slow rotator.

From the best obtained GP fit, we retrieved a rotation period of 144 ± 6 d, consistent with the rotation estimated from B_ℓ modulation (136 ± 13 d, Donati et al. 2023b) and that reported from $dTemp$ measurements ($P_{\text{rot}} = 153 \pm 3$ d Artigau et al. 2024). Those results demonstrate our ability to estimate rotational velocities from small-scale fields of low-activity stars, in spite of the relatively high uncertainty on magnetic field measurements and long rotation periods. Relying on the full set of data available for Barnard's star, we note that the convergence of the GP model on B_ℓ is challenging. In particular, we find that with wide uniform priors, the GP converges towards a low decay time (15 ± 13 d), a $P_{\text{rot}} = 134 \pm 50$ d, and a smoothing factor of 3.0 ± 1.9 . Setting the priors so that the decay time be larger than 50 (i.e. $\sim P_{\text{rot}}/3$), however, leads to convergence towards a decay time of 93 ± 40 d, a smoothing factor of 0.24 ± 0.15 and $P_{\text{rot}} = 189 \pm 54$ d. To help convergence, we fixed the decay time to 100 d, and the smoothing factor to 0.4 yielding $P_{\text{rot}} = 160 \pm 20$ d (see Table A.4). Simultaneously fitting two GPs with common P_{rot} to the $\langle B \rangle$ and B_ℓ data sets (see Fig. 5) yields a rotation period of 139 ± 5 d. The series of $\langle B \rangle$ and $|B_\ell|$

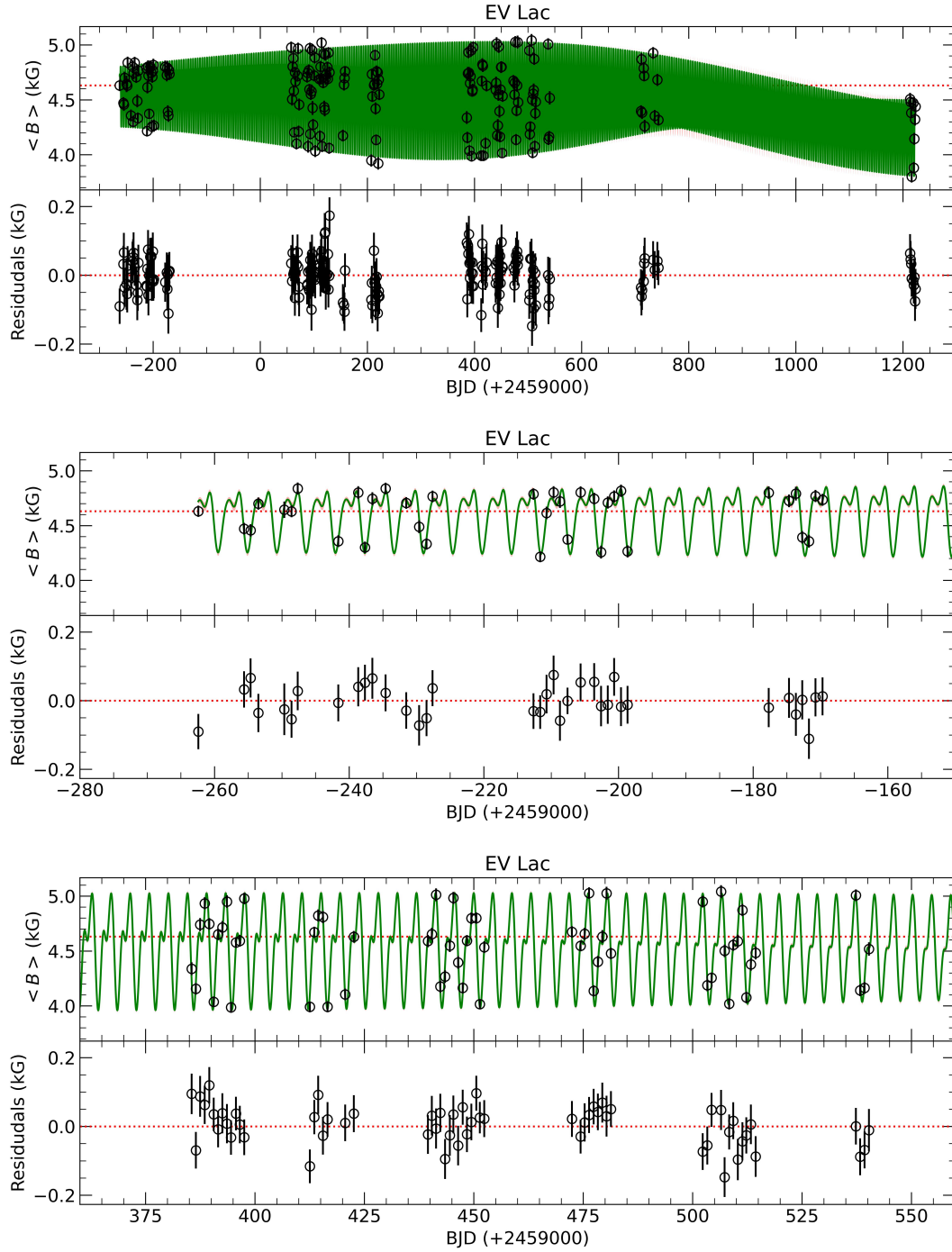


Fig. 3. Best fit GP fit (green) obtained on our small-scale magnetic fields measurements (black circles). The top panel shows the results obtained over our entire data set, while the middle and bottom panels are zoomed on different observation periods.

measurements appear uncorrelated, with a Pearson correlation coefficient of 0.12.

Here again, we run our process on the $dTemp$ measurements secured for Barnard's star, and obtained a well constrained rotation period $P_{\text{rot}} = 141 \pm 12$ d in excellent agreement with those derived from $\langle B \rangle$ and B_ℓ (see Fig. E.4, available on Zenodo).

4.6. PM J18482+0741

PM J18482+0741 is the second coolest target in our sample and a fully convective star, with a measured average magnetic field

of 1.27 ± 0.14 kG. We first apply our process with uninformed priors on the rotation period. For this star, the constraining P_{rot} is more challenging and multiple peaks are visible in the posterior distribution. To help convergence, we fix the decay time and smoothing to typical values of 300 and 1.50, respectively. We also adopt a Gaussian prior centered on the expected rotation period for this star with a standard deviation of 0.6 d (see Table A.5). With this prior, our process yields a rotation period of 2.762 ± 0.009 d. This estimate is in agreement with that derived from B_ℓ (2.761 ± 0.001 d) and by Díez Alonso et al. (2019, 2.76 ± 0.01 d).

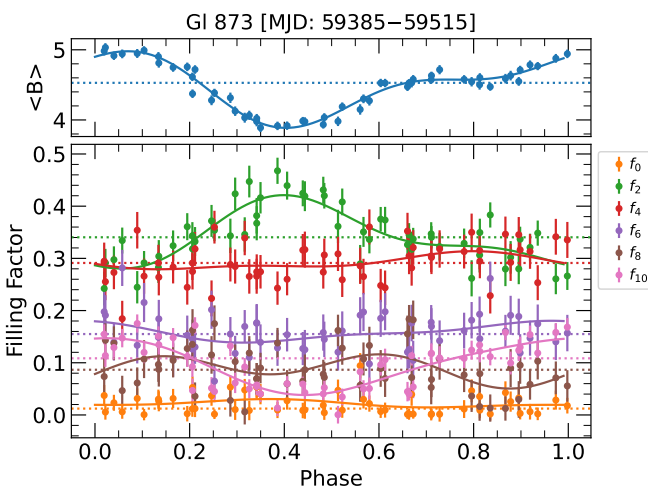


Fig. 4. Evolution of the filling factors distribution with respect to phase for EV Lac for observations recorded between MJD 59385 and 59515. Solid lines show a fit of a sinusoidal with a first harmonic to the data, assuming the rotation period obtained from our GP fit ($P_{\text{rot}} = 4.362$ d, see Sec. 4). For each filling factor, the dashed line marks the median of the series of points. Similar figures obtained for DS Leo, AD Leo, EV Lac, Barnard's star, PM J18482+0741 and CN Leo are presented in Fig. B.1, B.2, B.3, B.4, and B.5.

The mean value of $\langle B \rangle$ varies throughout the monitoring, with a maximum in mid-2022 (~ 1.5 kG) and a minimum in mid-2021 (~ 1.2 kG). This 0.3 kG is not negligible compared to the typical error on individual measurements of 0.2 kG. Furthermore, we observe that the amplitude of the rotationally modulated signal decreases in 2022 compared to the other semesters. For PM J18482+0741, the B_ℓ measurements do not show such long-term variations in amplitude nor mean, and appear uncorrelated to $\langle B \rangle$, with a Pearson coefficient of 0.14. The rotational modulation does not clearly appear in when fitting GP to time series of the magnetic filling factors.

Our simultaneous fit of two Gaussian processes to the $\langle B \rangle$ and B_ℓ data yields a rotation period of 2.759 ± 0.001 d, in very good agreement with that derived from $\langle B \rangle$ and B_ℓ (see Table A.5).

We carried out our process on the $dTemp$ measurements obtained for PM J18482+074 (see Fig. E.5, available on Zenodo). The convergence relying on wide uniform priors proves challenging and multiple peaks are observed in the posterior distribution, impacting our ability to clearly constrain the rotation period. To help convergence, we therefore fixed the smoothing factor to 1.50. A peak close to the highest likelihood is observed at about 2.7 d, consistent with the P_{rot} derived from $\langle B \rangle$ and B_ℓ , while several other peaks are observed in the posterior distribution (See Fig. G.17, available on Zenodo).

4.7. CN Leo (GI 406)

CN Leo is the coolest star in our sample, and one for which the uncertainties on $\langle B \rangle$ are the largest. These larger uncertainties can be attributed to the large molecular bands impacting the fits to the observed spectra. Using uninformed priors on stellar rotation leads to poor convergence of the GP fit. To help the fitting process, we fix the decay time and smoothing factor, and adopt a Gaussian prior centered on the expected rotation period (see Table A.6). Those additional constraints are not sufficient, however, to clearly detect the rotation period.

We find that our magnetic field estimates drop by ~ 0.3 kG from 2019 to 2022 (see Fig C.6, available on Zenodo). Those results could indicate the presence of a long-term periodic fluctuation with a half-period of $\sim 2\text{--}3$ yr. For this star, a clear rotational modulation is detected in the B_ℓ measurements, but the average B_ℓ values fluctuates by less than 0.2 kG and does not follow the variations observed in $\langle B \rangle$. For CN Leo, $\langle B \rangle$ and $|B_\ell|$ appear rather uncorrelated, with a Pearson correlation coefficient of -0.33 .

We repeat the analysis, simultaneously fitting two GPs to our $\langle B \rangle$ and B_ℓ datasets. We find that the process then quickly converges, yielding a rotation period of 2.700 ± 0.004 d, in excellent agreement with that obtained from B_ℓ (2.696 ± 0.006 d).

In addition, we perform a GP fit on the $dTemp$ measurements obtained for CN Leo, fixing the smoothing factor to 1.0 and setting a Gaussian prior on the rotation period to help convergence (see Table A.6 and Fig. E.6, available on Zenodo). A clear peak at the $P_{\text{rot}} = 3.003$ d is observed in the posterior distribution, while a secondary peak at about 2.4 d is also observed, de facto impacting the lower uncertainties on this value. We note that these values are not in agreement with that derived from B_ℓ measurements.

5. Comparison with $dTemp$

We compare our $\langle B \rangle$ estimates to $dTemp$ measurements obtained following Artigau et al. (2024). We find a clear anti-correlation between $\langle B \rangle$ and $dTemp$ for DS Leo, EV Lac, and Barnard's star with Pearson correlation coefficients of -0.93 , -0.86 , and -0.71 , respectively (see Figures 6, H.2, and H.3). No clear correlation is observed for AD Leo, CN Leo and PM J18482+0741 (correlation coefficients of -0.45 , 0.26 , and -0.33 , respectively). For CN Leo and PM J18482+0741, no clear rotational modulation is detected in the $dTemp$ measurements, which could result from the lower temperature and stronger molecular bands in their spectra. We also note that Artigau et al. (2024) obtained a -0.92 correlation between $\langle B \rangle$ and $dTemp$ for AU Mic, a M1V star exhibiting strong magnetic behavior.

We note that CN Leo and AD Leo, while the convergence of our GP fit to $dTemp$ is more challenging, a clear peak is observed at the expected rotation period in the posterior distribution. We perform linear fits to the $dTemp$ – $\langle B \rangle$ relations for Barnard's star, EV Lac and DS Leo, relying on orthogonal distance regression³, yielding slopes of -18.8 ± 0.8 , -19.8 ± 0.5 and -60.4 ± 2.5 K kG $^{-1}$, respectively. The intercept of these fits are of 8.2 ± 0.3 , 90.0 ± 2.3 and 53.0 ± 2.2 K for Barnard's star, EV Lac and DS Leo, respectively. These intercepts can be interpreted as the excess in effective temperature one would observe if the stars were not spotted.

We sum the effective temperatures reported in Table 2 and the intercepts derived above in order to compute the effective temperature of the stars if they were not spotted (T_{max}). Relying on the relation by Berdyugina (2005), we obtain contrast temperatures (between the photosphere and spots) of about 400, 520, and 720 K for Barnard's star, EV Lac and DS Leo, respectively. From T_{max} and the temperature of the spot (T_{spot}), we derive a fraction of spot coverage (f) for these three stars, assuming that $T_\star = (1 - f) T_{\text{max}} + f T_{\text{spot}}$ with T_\star the temperature reported in Table 2. Our results yield spot coverage fractions of about 2% for Barnard's star, 19% for EV Lac, and 8% for DS Leo. These results are consistent with EV Lac being the most magnetic star

³ implemented in Scipy

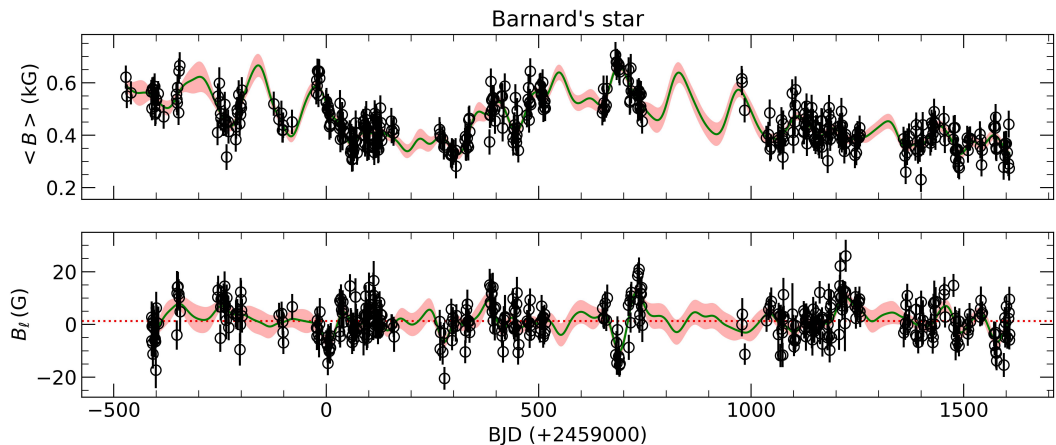


Fig. 5. Same as Fig. 1 for Barnard's star.

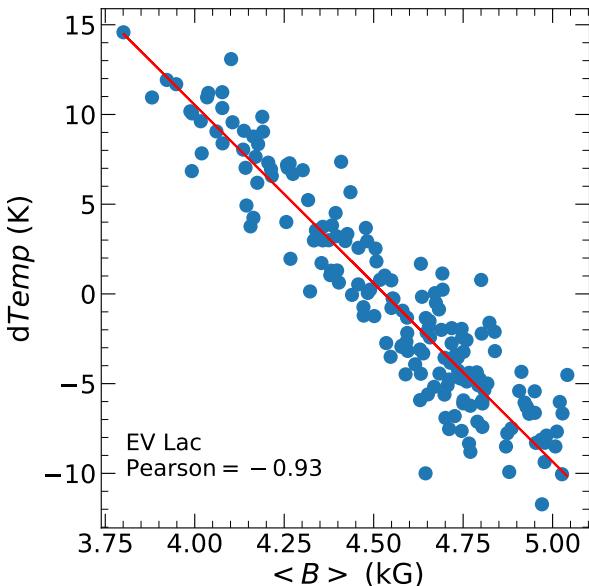


Fig. 6. Correlation between $\langle B \rangle$ and $dTemp$ for EV Lac. The red line shows a linear with slope $-19.8 \pm 0.5 \text{ K kG}^{-1}$ and intercept $90.0 \pm 2.3 \text{ K}$.

and Barnard's star being the least magnetic star of the three, although the reported fractions should be considered with caution given the numerous sources of uncertainties (Herbst et al. 2021).

6. Discussion and conclusions

In this paper, we presented the results of the first investigation of the small-scale magnetic field modulation of several stars. Our process relies on spectral models computed with Zee-Turbo (Cristofari et al. 2023a) and high-resolution near-infrared spectra recorded with SPIRou. Our sample is composed of 3 fully convective stars (CN Leo, PM J18482+0741 and Barnard's star), of 2 partially-convective star (AD Leo, DS Leo), and of EV Lac whose mass is close to the fully-convective boundary.

Our small scale-fields measurements reveal clear rotational modulation for EV Lac, DS Leo, and Barnard's star, with little prior assumptions on rotation period. With more drastic priors, we were able to obtain a rotation period for PM J18482+0741 but were unable to unambiguously constrain the rotation period

of CN Leo and AD Leo. Those results consolidate those previously obtained, for example on AU Mic (Donati et al. 2023a), showing that rotational period can be well constrained from $\langle B \rangle$, derived from unpolarized spectra, provided that the inclination of the targets is sufficiently large and the signal-to-noise ratio of the observations is high. Our sample included the low-activity Barnard's star, for which we retrieved a clear rotation period. These results demonstrate our ability to apply this technique to numerous additional targets monitored over the course of several years, including slow rotators.

In the case of EV Lac, we find a clear rotational modulation in the 2 and 10 kG components, while for the other stars the total magnetic flux variations are distributed on more components or restricted to the 2 kG component. These peculiar results for EV Lac could arise from the presence of large spots at the stellar surface (Ikuta et al. 2023, Larue et al. in prep), leading to clear modulation of the higher magnetic field component. Subsequent studies will explore the impact of large spots and magnetic topology on the distribution of filling factors.

We carried out joint fit of two Gaussian Processes to the $\langle B \rangle$ and B_ℓ measurements, with a single rotation period, decay time, and smoothing parameter. This approach has the potential to reduce error bars on P_{rot} estimates as the process can rely on additional information. This approach leads to quick and unambiguous convergence for most stars. We note that for PM J18482+0741, CN Leo and AD Leo, the P_{rot} estimates derived with this approach are very close to those obtained from the B_ℓ data set alone, with similar or larger error bars. This likely arises from the limited additional constraint provided by the $\langle B \rangle$ data set, for which sub-optimal fits are obtained. For the other stars, however, using both data sets provide additional constraints on the modeling of small-scale and large-scale magnetic fields.

Our measurements also reveal long-term variations of the small-scale magnetic fields, with amplitudes of the rotationally modulated signal that can increase by a factor of two (e.g. EV Lac, DS Leo) or average field strengths that can decrease by up to 0.3 kG (CN Leo). These fluctuations can be larger than the uncertainties computed on $\langle B \rangle$, and are therefore likely to impact precision measurements carried out on spectra recorded at a given epoch, or averaged over long periods of time.

We find no clear correlation between the time series of measurements of $\langle B \rangle$ and $|B_\ell|$ for any of the target in our sample. For DS Leo and EV Lac, variations in the signal amplitudes appear both in the $\langle B \rangle$ and B_ℓ measurements. Only for EV Lac and

AD Leo do the signals appear moderately anti-correlated or correlated, with Pearson correlation coefficient of -0.41 and 0.39 , respectively. For DS Leo, although $\langle B \rangle$ and $|B_\ell|$ appear uncorrelated, we note that the amplitude of both rotationally modulated time series vary. These variations appear asynchronous, which could indicate a different relation between the large-scale and small-scale magnetic fields for this star than for EV Lac.

We compared our obtained small-scale magnetic field measurements to $dTemp$ measurements obtained from the same SPIRou spectra. No clear correlation between the two sets of measurements was observed for AD Leo, which is seen pole on, and for Gl 406 and PM J18482+0741, for which no clear rotational modulation is found in the time series of $dTemp$ measurements. The comparison revealed clear anti-correlations between the two series of measurements for EV Lac, DS Leo and Barnard's star, with Pearson correlation coefficients below -0.8 . The anti-correlation between $\langle B \rangle$ and $dTemp$ likely indicates that the presence of strong magnetic fields can give rise to dark spots at the stellar surface. Comparing $\langle B \rangle$ and $dTemp$ for the three stars for which clear anti-correlations are observed, we note that $dTemp$ values vary more quickly with $\langle B \rangle$ for the M1 star (DS Leo), than for the later type M dwarfs. This observation is further supported by the rapid variation of $dTemp$ with $\langle B \rangle$ reported by Artigau et al. (2024) for the M1 star AU Mic. This phenomenon could be a consequence of the variation in spot coverage whose impact is more significant in earlier M dwarfs due to contrast. For EV Lac, we observe a significant decrease of the average small-scale magnetic field in September/October 2023. This change is accompanied by an increase in the average $dTemp$ measurements, suggesting that the lower field intensity drives a decrease in cool magnetic regions at the stellar surface. Continued monitoring of EV Lac will allow us to establish whether these changes are indicative of magnetic cycles and if the small-scale magnetic field has reached a minimum.

From linear fits to the $\langle B \rangle$ – $dTemp$ trends, we derived decreasing slopes with increasing contrast, consistent with the previous results suggesting that the contrast between the photosphere and spots increases with temperature (Berdyugina 2005), and suggesting that our measured small-scale magnetic field arise from spots at the stellar surface. We further deduced the effective temperature of the stars assuming that the obtained $\langle B \rangle$ are caused solely by spots. We relied on the relation proposed by Berdyugina (2005) to derive spot coverage estimates for Barnard's star, EV Lac and DS Leo. These results qualitatively agree with expectations, with the largest spot coverage (19%) for EV Lac, and the smallest (2%) for Barnard's star. The amplitude of the $dTemp$ signals suggest temporal fluctuations of the spot coverage by up to 5%. An in depth investigation of the relation between $\langle B \rangle$ and $dTemp$ should attempt to unambiguously establish the origin of these anti-correlations.

The results presented in this paper illustrate how much one can benefit from the small-scale magnetic fields measurements derived from nIR spectra collected over long observation campaigns. Future studies will provide additional measurements of small-scale magnetic fields and their temporal modulation. These measurements, along with longitudinal field measurements and large-scale magnetic field topology reconstructions, will help the community to build a more complete picture of M dwarfs magnetism above and below the fully convective limit. Small-scale magnetic field measurements will also be assets to mitigate their impact on radial-velocity curves (e.g., Haywood et al. 2016, 2022), in particular for slow rotating, relatively inactive stars, which are favored targets for the search for habitable exoplanets.

7. Data availability

Appendices C, D, E, F and G are available on Zenodo (<https://zenodo.org/records/16744873>).

Acknowledgements. This project received funding from the European Research Council (ERC, grant 740651, NewWorlds) under the innovation research and innovation program H2020. SB acknowledges funding by the Dutch Research Council (NWO) under the project "Exo-space weather and contemporaneous signatures of star-planet interactions" (with project number OCENW.M.22.215 of the research programme "Open Competition Domain Science- M"). XD acknowledges funding from the French National Research Agency in the framework of the Investissements d'Avenir program (ANR-15-IDEX-02), through the funding of the "Origin of Life" project of the Grenoble-Alpes University.

References

- Ambikasaran, S., Foreman-Mackey, D., Greengard, L., Hogg, D. W., & O'Neil, M. 2015, IEEE Transactions on Pattern Analysis and Machine Intelligence, 38, 252
- Angus, R., Morton, T., Aigrain, S., Foreman-Mackey, D., & Rajpaul, V. 2018, MNRAS, 474, 2094
- Artigau, É., Cadieux, C., Cook, N. J., et al. 2024, AJ, 168, 252
- Barnes, S. A. 2003, ApJ, 586, 464
- Bellotti, S., Morin, J., Lehmann, L. T., et al. 2023, A&A, 676, A56
- Bellotti, S., Morin, J., Lehmann, L. T., et al. 2024, A&A, 686, A66
- Bellotti, S., Petit, P., Morin, J., et al. 2022, A&A, 657, A107
- Berdyugina, S. V. 2005, Living Reviews in Solar Physics, 2, 8
- Bonfils, X., Lo Curto, G., Correia, A. C. M., et al. 2013, A&A, 556, A110
- Carmona, A., Delfosse, X., Ould-Elhkim, M., et al. 2025, A&A, in press, arXiv:2504.03572
- Chabrier, G. & Baraffe, I. 1997, A&A, 327, 1039
- Chabrier, G. & Küker, M. 2006, A&A, 446, 1027
- Cook, N. J., Artigau, É., Doyon, R., et al. 2022, PASP, 134, 114509
- Cristofari, P. I., Donati, J.-F., Folsom, C. P., et al. 2023a, MNRAS, 522, 1342
- Cristofari, P. I., Donati, J. F., Masseron, T., et al. 2022a, MNRAS, 516, 3802
- Cristofari, P. I., Donati, J. F., Masseron, T., et al. 2022b, MNRAS, 511, 1893
- Cristofari, P. I., Donati, J. F., Moutou, C., et al. 2023b, MNRAS, 526, 5648
- Díez Alonso, E., Caballero, J. A., Montes, D., et al. 2019, A&A, 621, A126
- Donati, J. F., Cristofari, P. I., Finocci, B., et al. 2023a, MNRAS, 525, 455
- Donati, J. F., Cristofari, P. I., Klein, B., Finocci, B., & Moutou, C. 2025, A&A, in press, arXiv:2507.01754
- Donati, J. F., Kouach, D., Moutou, C., et al. 2020, MNRAS, 498, 5684
- Donati, J. F. & Landstreet, J. D. 2009, ARA&A, 47, 333
- Donati, J. F., Lehmann, L. T., Cristofari, P. I., et al. 2023b, MNRAS, 525, 2015
- Donati, J. F., Morin, J., Petit, P., et al. 2008, MNRAS, 390, 545
- Donati, J. F., Semel, M., Carter, B. D., Rees, D. E., & Collier Cameron, A. 1997, MNRAS, 291, 658
- Dorn, R. J., Bristow, P., Smoker, J. V., et al. 2023, A&A, 671, A24
- Dressing, C. D. & Charbonneau, D. 2015, ApJ, 807, 45
- Dumusque, X., Cretignier, M., Sosnowska, D., et al. 2021, A&A, 648, A103
- Finocci, B., Donati, J. F., Cristofari, P. I., et al. 2023, MNRAS, 526, 4627
- Foreman-Mackey, D., Agol, E., Ambikasaran, S., & Angus, R. 2017, AJ, 154, 220
- Fouqué, P., Martioli, E., Donati, J. F., et al. 2023, A&A, 672, A52
- Gaidos, E., Mann, A. W., Kraus, A. L., & Ireland, M. 2016, MNRAS, 457, 2877
- Gustafsson, B., Edvardsson, B., Eriksson, K., et al. 2008, A&A, 486, 951
- Haywood, R. D., Collier Cameron, A., Unruh, Y. C., et al. 2016, MNRAS, 457, 3637
- Haywood, R. D., Milbourne, T. W., Saar, S. H., et al. 2022, ApJ, 935, 6
- Hébrard, É. M., Donati, J. F., Delfosse, X., et al. 2016, MNRAS, 461, 1465
- Herbst, K., Papaioannou, A., Airapetian, V. S., & Atri, D. 2021, ApJ, 907, 89
- Ikuta, K., Namekata, K., Notsu, Y., et al. 2023, ApJ, 948, 64
- Johns-Krull, C. M. & Valenti, J. A. 1996, ApJ, 459, L95
- Kochukhov, O. 2021, A&A Rev., 29, 1
- Kochukhov, O., Amarsi, A. M., Lavail, A., et al. 2024, A&A, 689, A36
- Kochukhov, O. & Lavail, A. 2017, ApJ, 835, L4
- Lavail, A., Kochukhov, O., & Wade, G. A. 2018, MNRAS, 479, 4836
- Mackey, A. D., Broby Nielsen, P., Ferguson, A. M. N., & Richardson, J. C. 2008, ApJ, 681, L17
- Marfil, E., Tabernero, H. M., Montes, D., et al. 2021, A&A, 656, A162
- Martioli, E., Hébrard, G., Fouqué, P., et al. 2022, A&A, 660, A86
- Morin, J., Donati, J. F., Petit, P., et al. 2008, MNRAS, 390, 567
- Passegger, V. M., Schweitzer, A., Shulyak, D., et al. 2019, A&A, 627, A161
- Pecaut, M. J. & Mamajek, E. E. 2013, ApJS, 208, 9

- Quirrenbach, A., Amado, P. J., Caballero, J. A., et al. 2014, in Society of Photo-Optical Instrumentation Engineers (SPIE) Conference Series, Vol. 9147, Ground-based and Airborne Instrumentation for Astronomy V, ed. S. K. Ramsay, I. S. McLean, & H. Takami, 91471F
- Rajpurohit, A. S., Allard, F., Rajpurohit, S., et al. 2018, A&A, 620, A180
- Rasmussen, C. E. & Williams, C. K. I. 2006, Gaussian Processes for Machine Learning
- Reiners, A., Shulyak, D., Käpylä, P. J., et al. 2022, A&A, 662, A41
- Reiners, A., Zechmeister, M., Caballero, J. A., et al. 2018, A&A, 612, A49
- Reylé, C., Jardine, K., Fouqué, P., et al. 2021, A&A, 650, A201
- Saar, S. H. & Linsky, J. L. 1985, ApJ, 299, L47
- Sarmento, P., Rojas-Ayala, B., Delgado Mena, E., & Blanco-Cuaresma, S. 2021, A&A, 649, A147
- Shulyak, D., Reiners, A., Engeln, A., et al. 2017, Nature Astronomy, 1, 0184
- Shulyak, D., Reiners, A., Seemann, U., Kochukhov, O., & Piskunov, N. 2014, A&A, 563, A35
- Skumanich, A. 1972, ApJ, 171, 565
- Vidotto, A. A., Gregory, S. G., Jardine, M., et al. 2014, MNRAS, 441, 2361
- Wende, S., Reiners, A., & Ludwig, H. G. 2009, A&A, 508, 1429
- Wright, N. J., Newton, E. R., Williams, P. K. G., Drake, J. J., & Yadav, R. K. 2018, MNRAS, 479, 2351
- Yadav, R. K., Christensen, U. R., Morin, J., et al. 2015, ApJ, 813, L31

Appendix A: Data tables

The results of the GP fits are presented in Tables A.1–A.6 (see Sec. 4). Tables A.7–A.12 present the $\langle B \rangle$ and $dTemp$ data used in this paper, and Tables A.13–A.18 present the B_ℓ data used in this paper (first entries, full table available at CDS).

Table A.1. GP hyper-parameters for DS Leo (Gl 410).

DS Leo	Value	Prior
GP fit on $\langle B \rangle$		
μ (kG)	$0.90^{+0.02}_{-0.02}$	$\mathcal{U}(-10, 10)$
σ (kG)	$0.01^{+0.01}_{-0.01}$	$\mathcal{U}(0, 1000)$
α (kG)	$0.08^{+0.01}_{-0.01}$	$\mathcal{U}(0, 10)$
l (d)	54^{+8}_{-7}	$\mathcal{U}(10, 500)$
β	$0.57^{+0.10}_{-0.08}$	$\mathcal{U}(0, 20)$
P_{rot} (d)	$13.953^{+0.088}_{-0.086}$	$\mathcal{U}(5, 20)$
χ^2_r	0.72	
RMS	0.02 (kG)	
GP fit on B_ℓ		
μ_ℓ (G)	$-0.60^{+3.24}_{-3.28}$	$\mathcal{U}(-500, 500)$
σ_ℓ (G)	$1.94^{+0.94}_{-1.16}$	$\mathcal{U}(0, 1000)$
α_ℓ (G)	$15.19^{+1.92}_{-1.60}$	$\mathcal{U}(0, 1000)$
l_ℓ (d)	57^{+9}_{-7}	$\mathcal{U}(10, 500)$
β_ℓ	$0.45^{+0.06}_{-0.05}$	$\mathcal{U}(0, 5)$
$P_{\text{rot},\ell}$ (d)	$14.001^{+0.077}_{-0.075}$	$\mathcal{U}(5, 20)$
$\chi^2_{r,\ell}$	0.66	
RMS _{ℓ}	3.93 (G)	
GP fit on $\langle B \rangle$ and B_ℓ		
μ (kG)	$0.90^{+0.02}_{-0.02}$	$\mathcal{U}(-10, 10)$
σ (kG)	$0.01^{+0.01}_{-0.01}$	$\mathcal{U}(0, 1000)$
α (kG)	$0.08^{+0.01}_{-0.01}$	$\mathcal{U}(0, 10)$
l (d)	54^{+8}_{-7}	$\mathcal{U}(10, 500)$
β	$0.57^{+0.10}_{-0.08}$	$\mathcal{U}(0, 20)$
P_{rot} (d)	$13.980^{+0.059}_{-0.058}$	$\mathcal{U}(5, 20)$
μ_ℓ (G)	$-0.76^{+3.31}_{-3.34}$	$\mathcal{U}(-500, 500)$
σ_ℓ (G)	$1.90^{+0.97}_{-1.14}$	$\mathcal{U}(0, 1000)$
α_ℓ (G)	$15.48^{+1.98}_{-1.61}$	$\mathcal{U}(0, 1000)$
l_ℓ (d)	58^{+9}_{-7}	$\mathcal{U}(10, 500)$
β_ℓ	$0.45^{+0.06}_{-0.05}$	$\mathcal{U}(0, 20)$
χ^2_r	0.72	
$\chi^2_{r,\ell}$	0.66	
RMS	0.02 (kG)	
RMS _{ℓ}	3.94 (G)	
GP fit on $dTemp$		
μ_{dTemp} (K)	$-1.18^{+1.57}_{-1.61}$	$\mathcal{U}(-50, 50)$
σ_{dTemp} (K)	$0.71^{+0.13}_{-0.12}$	$\mathcal{U}(0, 1000)$
α_{dTemp} (K)	$7.46^{+0.93}_{-0.81}$	$\mathcal{U}(0, 100)$
l_{dTemp} (d)	38^{+3}_{-3}	$\mathcal{U}(10, 500)$
β_{dTemp}	$0.63^{+0.07}_{-0.06}$	$\mathcal{U}(0, 20)$
$P_{\text{rot},dTemp}$ (d)	$14.214^{+0.106}_{-0.102}$	$\mathcal{U}(3, 200)$
$\chi^2_{r,dTemp}$	0.98	
RMS _{$dTemp$}	0.58 (K)	

Notes. Hyper-parameters obtained when applying our process to the small-scale magnetic field measurements ($\langle B \rangle$), the longitudinal magnetic field (B_ℓ), or $\langle B \rangle$ and B_ℓ simultaneously. Error bars on $\langle B \rangle$ and $dTemp$ measurements were adjusted to ensure a minimum reduced χ^2 close to one for the best fit.

Table A.2. Same as Table A.1 for AD Leo (Gl 388).

AD Leo	Value	Prior
GP fit on $\langle B \rangle$		
μ (kG)	$3.22^{+0.08}_{-0.07}$	$\mathcal{U}(-10, 10)$
σ (kG)	$0.01^{+0.01}_{-0.01}$	$\mathcal{U}(0, 1000)$
α (kG)	$0.09^{+0.07}_{-0.04}$	$\mathcal{U}(0, 10)$
l (d)	300	Fixed
β	1.50	Fixed
P_{rot} (d)	$2.232^{+0.095}_{-0.148}$	$\mathcal{G}(2.23, 0.20)$
χ^2_r	0.74	
RMS	0.05 (kG)	
GP fit on B_ℓ		
μ_ℓ (G)	$-164.94^{+118.82}_{-131.02}$	$\mathcal{U}(-1000, 1000)$
σ_ℓ (G)	$5.02^{+3.50}_{-3.58}$	$\mathcal{U}(0, 1000)$
α_ℓ (G)	$79.87^{+114.76}_{-68.58}$	$\mathcal{U}(0, 1000)$
l_ℓ (d)	254^{+105}_{-93}	$\mathcal{U}(10, 500)$
β_ℓ	$1.42^{+1.32}_{-0.94}$	$\mathcal{U}(0, 5)$
$P_{\text{rot},\ell}$ (d)	$2.230^{+0.001}_{-0.001}$	$\mathcal{U}(2, 5)$
$\chi^2_{r,\ell}$	0.94	
RMS _{ℓ}	15.58 (G)	
GP fit on $\langle B \rangle$ and B_ℓ		
μ (kG)	$3.22^{+0.08}_{-0.08}$	$\mathcal{U}(-10, 10)$
σ (kG)	$0.02^{+0.01}_{-0.01}$	$\mathcal{U}(0, 1000)$
α (kG)	$0.09^{+0.07}_{-0.04}$	$\mathcal{U}(0, 10)$
l (d)	300	Fixed
β	1.50	Fixed
P_{rot} (d)	$2.230^{+0.001}_{-0.001}$	$\mathcal{U}(1, 5)$
μ_ℓ (G)	$-157.84^{+134.94}_{-147.75}$	$\mathcal{U}(-1000, 1000)$
σ_ℓ (G)	$5.74^{+3.49}_{-3.89}$	$\mathcal{U}(0, 1000)$
α_ℓ (G)	$98.77^{+157.32}_{-85.53}$	$\mathcal{U}(0, 1000)$
l_ℓ (d)	282^{+157}_{-111}	$\mathcal{U}(10, 800)$
β_ℓ	$1.67^{+1.45}_{-1.05}$	$\mathcal{U}(0, 5)$
χ^2_r	0.75	
$\chi^2_{r,\ell}$	0.81	
RMS	0.05 (kG)	
RMS _{ℓ}	14.75 (G)	
GP fit on $dTemp$		
μ_{dTemp} (K)	$0.21^{+1.17}_{-1.17}$	$\mathcal{U}(-20, 20)$
σ_{dTemp} (K)	$0.49^{+0.20}_{-0.24}$	$\mathcal{U}(0, 1000)$
α_{dTemp} (K)	$2.60^{+0.68}_{-0.51}$	$\mathcal{U}(0, 20)$
l_{dTemp} (d)	82^{+24}_{-25}	$\mathcal{U}(10, 400)$
β_{dTemp}	1.50	Fixed
$P_{\text{rot},dTemp}$ (d)	$2.227^{+0.010}_{-0.015}$	$\mathcal{G}(2.30, 0.20)$
$\chi^2_{r,dTemp}$	1.01	
RMS _{$dTemp$}	0.89 (K)	

Table A.3. Same as Table A.1 for EV Lac (Gl 873).

EV Lac	Value	Prior
GP fit on $\langle B \rangle$		
μ (kG)	$4.42^{+0.19}_{-0.21}$	$\mathcal{U}(0, 10)$
σ (kG)	$0.02^{+0.01}_{-0.01}$	$\mathcal{U}(0, 1000)$
α (kG)	$0.34^{+0.14}_{-0.09}$	$\mathcal{U}(0, 10)$
l (d)	438^{+69}_{-73}	$\mathcal{U}(100, 800)$
β	$0.60^{+0.13}_{-0.11}$	$\mathcal{U}(0, 10)$
P_{rot} (d)	$4.362^{+0.001}_{-0.001}$	$\mathcal{U}(0, 10)$
χ^2_r	0.92	
RMS	0.05 (kG)	
GP fit on B_ℓ		
μ_ℓ (G)	$-69.61^{+58.73}_{-58.77}$	$\mathcal{U}(-500, 500)$
σ_ℓ (G)	$6.74^{+6.00}_{-5.67}$	$\mathcal{U}(0, 1000)$
α_ℓ (G)	$181.48^{+33.44}_{-26.57}$	$\mathcal{U}(0, 1000)$
l_ℓ (d)	127^{+15}_{-13}	$\mathcal{U}(10, 500)$
β_ℓ	$0.48^{+0.06}_{-0.06}$	$\mathcal{U}(0, 3)$
$P_{\text{rot},\ell}$ (d)	$4.371^{+0.003}_{-0.003}$	$\mathcal{U}(3, 10)$
$\chi^2_{r,\ell}$	0.69	
RMS $_\ell$	26.39 (G)	
GP fit on $\langle B \rangle$ and B_ℓ		
μ (kG)	$4.42^{+0.20}_{-0.21}$	$\mathcal{U}(0, 10)$
σ (kG)	$0.01^{+0.01}_{-0.01}$	$\mathcal{U}(0, 1000)$
α (kG)	$0.35^{+0.15}_{-0.10}$	$\mathcal{U}(0, 1000)$
l (d)	440^{+81}_{-132}	$\mathcal{U}(10, 800)$
β	$0.59^{+0.14}_{-0.11}$	$\mathcal{U}(0, 10)$
P_{rot} (d)	$4.363^{+0.001}_{-0.001}$	$\mathcal{U}(0, 10)$
μ_ℓ (G)	$-81.99^{+70.28}_{-71.74}$	$\mathcal{U}(-500, 500)$
σ_ℓ (G)	$9.37^{+5.49}_{-6.18}$	$\mathcal{U}(0, 1000)$
α_ℓ (G)	$191.74^{+40.29}_{-31.22}$	$\mathcal{U}(0, 1000)$
l_ℓ (d)	127^{+14}_{-13}	$\mathcal{U}(10, 800)$
β_ℓ	$0.54^{+0.07}_{-0.06}$	$\mathcal{U}(0, 10)$
χ^2_r	0.92	
$\chi^2_{r,\ell}$	0.77	
RMS	0.05 (kG)	
RMS $_\ell$	27.64 (G)	
GP fit on dTemp		
μ_{dTemp} (K)	$1.18^{+1.73}_{-1.44}$	$\mathcal{U}(0, 10)$
σ_{dTemp} (K)	$0.53^{+0.21}_{-0.26}$	$\mathcal{U}(0, 1000)$
α_{dTemp} (K)	$6.25^{+1.61}_{-1.32}$	$\mathcal{U}(0, 10)$
l_{dTemp} (d)	460^{+92}_{-84}	$\mathcal{U}(100, 800)$
β_{dTemp}	$0.50^{+0.09}_{-0.07}$	$\mathcal{U}(0, 10)$
$P_{\text{rot,dTemp}}$ (d)	$4.362^{+0.001}_{-0.001}$	$\mathcal{U}(0, 10)$
$\chi^2_{r,\text{dTemp}}$	0.90	
RMS $_{\text{dTemp}}$	1.28 (K)	

Table A.4. Same as Table A.1 for Barnard's star (Gl 699).

Barnard's star	Value	Prior
GP fit on $\langle B \rangle$		
μ (kG)	$0.46^{+0.05}_{-0.05}$	$\mathcal{U}(-10, 10)$
σ (kG)	$0.00^{+0.00}_{-0.00}$	$\mathcal{U}(0, 1000)$
α (kG)	$0.10^{+0.05}_{-0.03}$	$\mathcal{U}(0, 10)$
l (d)	222^{+58}_{-50}	$\mathcal{U}(50, 500)$
β	$1.10^{+0.76}_{-0.44}$	$\mathcal{U}(0, 20)$
P_{rot} (d)	144^{+6}_{-6}	$\mathcal{U}(50, 200)$
χ^2_r	0.91	
RMS	0.08 (kG)	
GP fit on B_ℓ		
μ_ℓ (G)	$1.54^{+1.18}_{-1.17}$	$\mathcal{U}(-500, 500)$
σ_ℓ (G)	$2.13^{+0.42}_{-0.48}$	$\mathcal{U}(0, 1000)$
α_ℓ (G)	$5.40^{+0.69}_{-0.63}$	$\mathcal{U}(0, 1000)$
l_ℓ (d)	100	Fixed
β_ℓ	0.40	Fixed
$P_{\text{rot},\ell}$ (d)	$159.226^{+15.785}_{-19.423}$	$\mathcal{U}(50, 200)$
$\chi^2_{r,\ell}$	1.09	
RMS $_\ell$	5.00 (G)	
GP fit on $\langle B \rangle$ and B_ℓ		
μ (kG)	$0.47^{+0.03}_{-0.03}$	$\mathcal{U}(-10, 10)$
σ (kG)	$0.00^{+0.00}_{-0.00}$	$\mathcal{U}(0, 1000)$
α (kG)	$0.09^{+0.02}_{-0.01}$	$\mathcal{U}(0, 10)$
l (d)	181^{+32}_{-35}	$\mathcal{U}(10, 800)$
β	$0.66^{+0.17}_{-0.12}$	$\mathcal{U}(0, 20)$
P_{rot} (d)	139^{+5}_{-4}	$\mathcal{U}(50, 200)$
μ_ℓ (G)	$1.62^{+1.22}_{-1.18}$	$\mathcal{U}(-1000, 1000)$
σ_ℓ (G)	$1.96^{+0.48}_{-0.57}$	$\mathcal{U}(0, 1000)$
α_ℓ (G)	$5.24^{+0.68}_{-0.59}$	$\mathcal{U}(0, 1000)$
l_ℓ (d)	100	Fixed
β_ℓ	0.40	Fixed
χ^2_r	0.81	
$\chi^2_{r,\ell}$	1.08	
RMS	0.08 (kG)	
RMS $_\ell$	4.98 (G)	
GP fit on dTemp		
μ_{dTemp} (K)	$-0.29^{+0.26}_{-0.26}$	$\mathcal{U}(-50, 50)$
σ_{dTemp} (K)	$0.17^{+0.05}_{-0.07}$	$\mathcal{U}(0, 1000)$
α_{dTemp} (K)	$1.06^{+0.15}_{-0.12}$	$\mathcal{U}(0, 100)$
l_{dTemp} (d)	116^{+22}_{-24}	$\mathcal{U}(50, 500)$
β_{dTemp}	$0.49^{+0.12}_{-0.09}$	$\mathcal{U}(0, 5)$
$P_{\text{rot,dTemp}}$ (d)	$141.058^{+6.603}_{-11.625}$	$\mathcal{U}(50, 200)$
$\chi^2_{r,\text{dTemp}}$	0.99	
RMS $_{\text{dTemp}}$	0.47 (K)	

Table A.5. Same as Table A.1 for PM J18482+0741.

PM J18482+0741	Value	Prior
GP fit on $\langle B \rangle$		
μ (kG)	$1.55^{+0.11}_{-0.11}$	$\mathcal{U}(-10, 10)$
σ (kG)	$0.01^{+0.02}_{-0.01}$	$\mathcal{U}(0, 1000)$
α (kG)	$0.15^{+0.06}_{-0.05}$	$\mathcal{U}(0, 10)$
l (d)	113^{+33}_{-31}	$\mathcal{U}(10, 500)$
β	1.50	Fixed
P_{rot} (d)	$2.762^{+0.009}_{-0.007}$	$\mathcal{G}(2.76, 0.60)$
χ^2_r	0.89	
RMS	0.09 (kG)	
GP fit on B_ℓ		
μ_ℓ (G)	$-6.20^{+92.85}_{-91.69}$	$\mathcal{U}(-1000, 1000)$
σ_ℓ (G)	$8.40^{+3.30}_{-4.10}$	$\mathcal{U}(0, 1000)$
α_ℓ (G)	$44.18^{+126.91}_{-60.46}$	$\mathcal{U}(0, 400)$
l_ℓ (d)	650^{+177}_{-261}	$\mathcal{U}(10, 1000)$
β_ℓ	$0.35^{+1.30}_{-0.76}$	$\mathcal{U}(0, 5)$
$P_{\text{rot},\ell}$ (d)	$2.761^{+0.001}_{-0.001}$	$\mathcal{U}(2, 5)$
$\chi^2_{r,\ell}$	1.00	
RMS $_\ell$	19.64 (G)	
GP fit on $\langle B \rangle$ and B_ℓ		
μ (kG)	$1.55^{+0.31}_{-0.68}$	$\mathcal{U}(-10, 10)$
σ (kG)	$0.01^{+0.02}_{-0.01}$	$\mathcal{U}(0, 1000)$
α (kG)	$0.15^{+1.40}_{-0.34}$	$\mathcal{U}(0, 5)$
l (d)	112^{+100}_{-67}	$\mathcal{U}(10, 500)$
β	$1.23^{+14.47}_{-3.43}$	$\mathcal{U}(0, 50)$
P_{rot} (d)	$2.759^{+0.002}_{-0.002}$	$\mathcal{U}(2, 5)$
μ_ℓ (G)	$-12.02^{+56.52}_{-59.46}$	$\mathcal{U}(-1000, 1000)$
σ_ℓ (G)	$11.47^{+3.06}_{-3.48}$	$\mathcal{U}(0, 1000)$
α_ℓ (G)	$81.00^{+24.94}_{-18.59}$	$\mathcal{U}(0, 400)$
l_ℓ (d)	300	Fixed
β_ℓ	1.00	Fixed
χ^2_r	0.85	
$\chi^2_{r,\ell}$	1.17	
RMS	0.09 (kG)	
RMS $_\ell$	20.50 (G)	
GP fit on dTemp		
μ_{dTemp} (K)	$-2.36^{+3.54}_{-3.80}$	$\mathcal{U}(-50, 50)$
σ_{dTemp} (K)	$0.37^{+0.56}_{-0.59}$	$\mathcal{U}(0, 1000)$
α_{dTemp} (K)	$4.11^{+3.11}_{-1.57}$	$\mathcal{U}(0, 100)$
l_{dTemp} (d)	300	Fixed
β_{dTemp}	1.50	Fixed
$P_{\text{rot,dTemp}}$ (d)	$2.771^{+1.426}_{-1.216}$	$\mathcal{U}(2, 5)$
$\chi^2_{r,\text{dTemp}}$	0.98	
RMS $_{\text{dTemp}}$	3.16 (K)	

Table A.6. Same as Table A.1 for CN Leo (Gl 406).

CN Leo	Value	Prior
GP fit on $\langle B \rangle$		
μ (kG)	$3.30^{+0.06}_{-0.06}$	$\mathcal{U}(-10, 10)$
σ (kG)	$0.01^{+0.01}_{-0.01}$	$\mathcal{U}(0, 1000)$
α (kG)	$0.09^{+0.03}_{-0.02}$	$\mathcal{U}(0, 10)$
l (d)	300	Fixed
β	1.50	Fixed
P_{rot} (d)	2.694*	$\mathcal{G}(2.70, 0.30)$
χ^2_r	0.89	
RMS	0.15 (kG)	
GP fit on B_ℓ		
μ_ℓ (G)	$-622.91^{+93.31}_{-104.48}$	$\mathcal{U}(-1000, 1000)$
σ_ℓ (G)	$7.70^{+8.55}_{-8.05}$	$\mathcal{U}(0, 1000)$
α_ℓ (G)	$107.30^{+138.78}_{-76.88}$	$\mathcal{U}(0, 1000)$
l_ℓ (d)	99^{+35}_{-49}	$\mathcal{U}(10, 500)$
β_ℓ	$1.74^{+2.56}_{-1.36}$	$\mathcal{U}(0, 10)$
$P_{\text{rot},\ell}$ (d)	$2.696^{+0.004}_{-0.006}$	$\mathcal{U}(2, 4)$
$\chi^2_{r,\ell}$	0.88	
RMS $_\ell$	53.53 (G)	
GP fit on $\langle B \rangle$ and B_ℓ		
μ (kG)	$3.31^{+0.19}_{-0.20}$	$\mathcal{U}(-10, 10)$
σ (kG)	$0.01^{+0.01}_{-0.01}$	$\mathcal{U}(0, 1000)$
α (kG)	$0.17^{+0.22}_{-0.12}$	$\mathcal{U}(0, 10)$
l (d)	498^{+263}_{-221}	$\mathcal{U}(10, 1000)$
β	$7.56^{+5.85}_{-5.48}$	$\mathcal{U}(0, 20)$
P_{rot} (d)	$2.700^{+0.002}_{-0.004}$	$\mathcal{U}(2, 5)$
μ_ℓ (G)	$-649.35^{+103.79}_{-116.08}$	$\mathcal{U}(-1000, 1000)$
σ_ℓ (G)	$10.26^{+9.54}_{-8.98}$	$\mathcal{U}(0, 1000)$
α_ℓ (G)	$163.57^{+157.74}_{-88.07}$	$\mathcal{U}(0, 1000)$
l_ℓ (d)	151^{+34}_{-42}	$\mathcal{U}(10, 1000)$
β_ℓ	$2.78^{+2.64}_{-1.59}$	$\mathcal{U}(0, 10)$
χ^2_r	0.93	
$\chi^2_{r,\ell}$	0.94	
RMS	0.15 (kG)	
RMS $_\ell$	54.59 (G)	
GP fit on dTemp		
μ_{dTemp} (K)	$0.20^{+0.43}_{-0.43}$	$\mathcal{U}(-1000, 1000)$
σ_{dTemp} (K)	$0.68^{+0.28}_{-0.35}$	$\mathcal{U}(0, 1000)$
α_{dTemp} (K)	$1.53^{+0.36}_{-0.29}$	$\mathcal{U}(0, 1000)$
l_{dTemp} (d)	45^{+15}_{-13}	$\mathcal{U}(10, 500)$
β_{dTemp}	1.00	Fixed
$P_{\text{rot,dTemp}}$ (d)	$3.003^{+0.031}_{-0.536}$	$\mathcal{G}(2.70, 0.30)$
$\chi^2_{r,\text{dTemp}}$	1.02	
RMS $_{\text{dTemp}}$	1.78 (K)	

Notes. * Value corresponding to the maximum of likelihood in the posterior distribution. The posterior distribution shows multiple peaks that does not allow us to extract satisfactory error bars.

Table A.7. Measurements obtained each night for DS Leo (abstract Table).

MJD	$\langle B \rangle$ (kG)	f_0 (%)	f_2 (%)	f_4 (%)	f_6 (%)	f_8 (%)	f_{10} (%)	dTemp (K)
59157.6134	1.03 ± 0.03	51.6 ± 1.5	45.7 ± 2.0	2.4 ± 1.2	0.1 ± 0.3	0.1 ± 0.2	0.0 ± 0.1	-10.11 ± 0.41
59158.6077	1.08 ± 0.03	48.9 ± 1.5	48.4 ± 1.9	2.4 ± 1.1	0.2 ± 0.4	0.1 ± 0.2	0.0 ± 0.1	-13.46 ± 0.41
59207.5509	0.97 ± 0.04	54.5 ± 2.0	43.2 ± 2.5	1.6 ± 1.2	0.5 ± 0.6	0.1 ± 0.3	0.1 ± 0.2	3.54 ± 0.49

Notes. The complete table is available online in machine readable format.

Table A.8. Same as Table A.7 for EV Lac

MJD	$\langle B \rangle$ (kG)	f_0 (%)	f_2 (%)	f_4 (%)	f_6 (%)	f_8 (%)	f_{10} (%)	dTemp (K)
58737.5820	4.63 ± 0.05	1.5 ± 4.0	28.8 ± 3.0	30.0 ± 4.8	20.1 ± 5.4	16.3 ± 4.5	3.3 ± 2.4	-4.45 ± 1.53
58744.3863	4.47 ± 0.05	1.8 ± 4.1	35.9 ± 3.2	25.2 ± 4.8	20.5 ± 5.3	7.6 ± 4.7	9.0 ± 2.7	-0.74 ± 1.49
58745.3476	4.46 ± 0.06	1.2 ± 4.5	31.8 ± 3.2	36.0 ± 5.2	12.4 ± 6.0	10.6 ± 5.2	7.9 ± 2.9	0.53 ± 1.89

Table A.9. Same as Table A.7 for AD Leo

MJD	$\langle B \rangle$ (kG)	f_0 (%)	f_2 (%)	f_4 (%)	f_6 (%)	f_8 (%)	f_{10} (%)	dTemp (K)
58528.5699	3.26 ± 0.07	0.9 ± 1.7	51.7 ± 3.3	33.4 ± 4.3	12.0 ± 3.7	1.6 ± 1.9	0.4 ± 0.8	-2.06 ± 0.94
58530.4672	3.40 ± 0.06	0.3 ± 1.0	49.4 ± 2.8	34.3 ± 4.3	12.4 ± 4.0	3.3 ± 2.3	0.4 ± 0.8	-3.09 ± 0.91
58531.6235	3.34 ± 0.07	1.2 ± 2.0	52.0 ± 3.3	32.6 ± 4.1	7.5 ± 4.1	6.2 ± 2.7	0.5 ± 1.1	1.20 ± 0.94

Table A.10. Same as Table A.7 for CN Leo

MJD	$\langle B \rangle$ (kG)	f_0 (%)	f_2 (%)	f_4 (%)	f_6 (%)	f_8 (%)	f_{10} (%)	dTemp (K)
58528.5993	3.51 ± 0.08	14.4 ± 7.8	46.8 ± 12.0	12.4 ± 9.5	11.2 ± 8.7	13.1 ± 6.6	2.0 ± 2.2	-0.76 ± 2.27
58530.5844	3.37 ± 0.08	15.2 ± 8.1	45.6 ± 12.9	14.5 ± 10.7	13.5 ± 9.1	9.5 ± 6.1	1.7 ± 1.8	-7.09 ± 2.14
58531.6429	5.01 ± 0.48	35.7 ± 13.6	13.2 ± 13.5	11.8 ± 13.0	13.0 ± 13.8	13.9 ± 14.1	12.4 ± 13.6	4.77 ± 2.30

Table A.11. Same as Table A.7 for PMJ 18482+0741

MJD	$\langle B \rangle$ (kG)	f_0 (%)	f_2 (%)	f_4 (%)	f_6 (%)	f_8 (%)	f_{10} (%)	dTemp (K)
59296.5872	1.66 ± 0.09	34.5 ± 3.0	58.6 ± 8.2	3.3 ± 3.2	2.0 ± 1.8	1.0 ± 1.1	0.6 ± 0.6	-1.65 ± 3.08
59297.6055	1.60 ± 0.08	32.3 ± 2.6	63.0 ± 7.8	2.5 ± 2.5	1.2 ± 1.3	0.7 ± 0.7	0.4 ± 0.5	-5.63 ± 2.78
59304.6175	1.59 ± 0.09	36.9 ± 3.0	56.7 ± 8.5	3.1 ± 3.0	1.7 ± 1.7	1.1 ± 1.1	0.6 ± 0.6	-1.13 ± 3.33

Table A.12. Same as Table A.7 for Barnard's star

MJD	$\langle B \rangle$ (kG)	f_0 (%)	f_2 (%)	f_4 (%)	f_6 (%)	f_8 (%)	f_{10} (%)	dTemp (K)
58528.6717	0.62 ± 0.04	68.9 ± 3.9	31.1 ± 3.9	0.0 ± 0.0	0.0 ± 0.0	0.0 ± 0.0	0.0 ± 0.0	-1.34 ± 0.50
58530.6687	0.55 ± 0.05	72.5 ± 4.0	27.5 ± 4.0	0.0 ± 0.0	0.0 ± 0.0	0.0 ± 0.0	0.0 ± 0.0	-1.85 ± 0.24
58540.6805	0.56 ± 0.04	71.9 ± 3.9	28.1 ± 3.9	0.0 ± 0.0	0.0 ± 0.0	0.0 ± 0.0	0.0 ± 0.0	-2.64 ± 0.20

Table A.13. B_ℓ measurements obtained each night for DS Leo (abstract Table). The complete table is available at CDS.

MJD	B_ℓ (G)
59157.6116	-10.66 ± 4.82
59158.6059	1.14 ± 4.72
59207.5537	-3.18 ± 4.77

Table A.14. Same as Table A.7 for EV Lac

MJD	B_ℓ (G)
58737.5865	128.63 ± 33.70
58744.3908	-186.34 ± 32.31
58745.3521	62.20 ± 34.57

Table A.15. Same as Table A.7 for AD Leo

MJD	B_ℓ (G)
58588.2634	-223.42 ± 17.46
58589.5079	-199.36 ± 20.36
58591.3814	-217.51 ± 17.10

Table A.16. Same as Table A.7 for CN Leo

MJD	B_ℓ (G)
58589.5176	-739.23 ± 87.44
58591.3895	-851.25 ± 68.78
58592.4557	-623.14 ± 74.71

Table A.17. Same as Table A.7 for PMJ 18482+0741

MJD	B_ℓ (G)
59296.5882	-82.98 ± 21.45
59297.6060	14.88 ± 18.11
59304.6186	-42.17 ± 26.33

Table A.18. Same as Table A.7 for Barnard's star

MJD	B_ℓ (G)
58588.6111	-6.13 ± 5.91
58588.6163	2.76 ± 5.97
58589.6243	-0.69 ± 6.22

Appendix B: filling factors distribution

Figures B.1, B.2, B.3, B.4, and B.5 present the phase folded modulation of the magnetic filling factors DS Leo, AD Leo, Barnard's star, PMJ J18482+0741 and CN Leo, respectively.

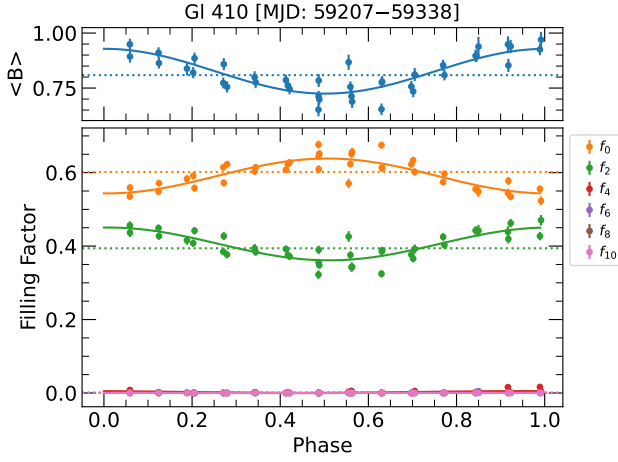


Fig. B.1. Same as Fig. 4 for DS Leo, assuming $P_{\text{rot}} = 13.982$ d, for observations recorded between MJD 59207 and 59338.

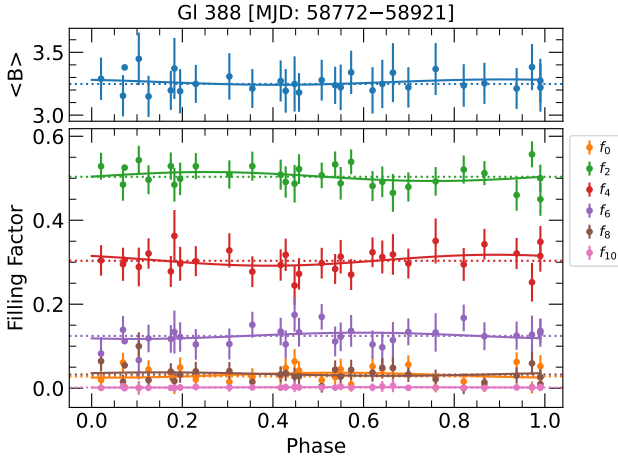


Fig. B.2. Same as Fig. 4 for AD Leo, assuming $P_{\text{rot}} = 2.230$ d, for observations recorded between MJD 58772 and 58921.

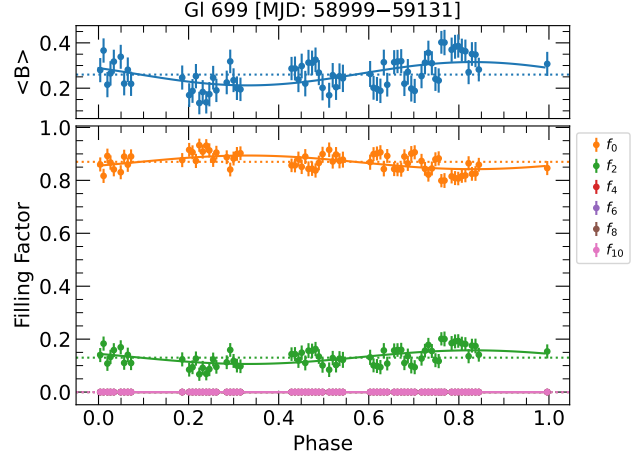


Fig. B.3. Same as Fig. 4 for Barnard's star, assuming $P_{\text{rot}} = 131.472$ d, for observations recorded between MJD 58999 and 59131.

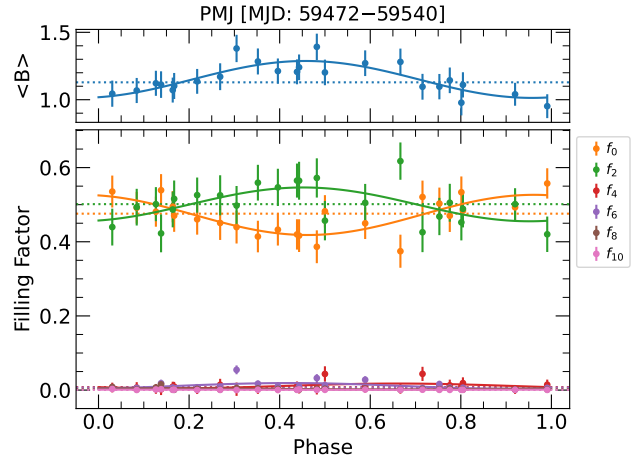


Fig. B.4. Same as Fig. 4 for PMJ J18482+0741, assuming $P_{\text{rot}} = 2.760$ d, for observations recorded between MJD 59472 and 59540.

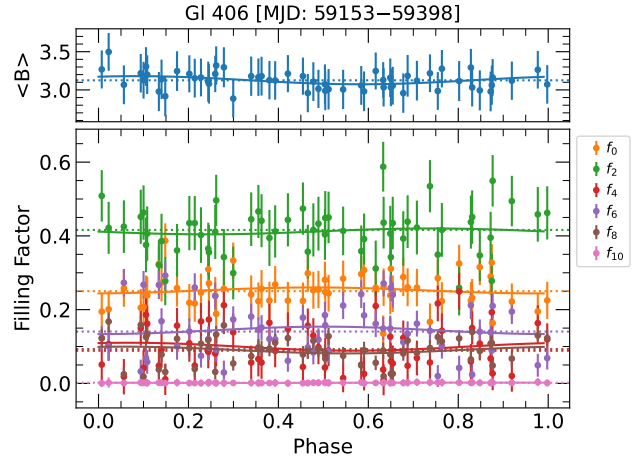


Fig. B.5. Same as Fig. 4 for CN Leo, assuming $P_{\text{rot}} = 2.696$ d, for observations recorded between MJD 59153 and 59398.